ACS Energy LETTERS

http://pubs.acs.org/journal/aelccp

LETTER

Structural Deformation Controls Charge Losses in $MAPbI_3$: Unsupervised Machine Learning of Nonadiabatic Molecular Dynamics

Guoqing Zhou, Weibin Chu, and Oleg V. Prezhdo*

Cite This: *ACS Energy Lett.* 2020, 5, 1930−1938

Read Online

ACCESS | Metrics & More | Article Recommendations | Supporting Information

ABSTRACT: The rapid increase in perovskite solar cell efficiencies has motivated massive experimental and theoretical efforts aimed at understanding and enhancing the performance. We apply machine learning to nonadiabatic molecular dynamics simulation of nonradiative charge recombination in $MAPbI_3$ and discover that the I−I−I angle is the key structural parameter governing nonadiabatic electron−phonon coupling and the bandgap. Surprisingly, the structure of $MAPbI_3$ is much more important that the motions of $MAPbI_3$, even though the coupling depends explicitly on nuclear velocity. Also surprisingly, rotational and center-of-mass motions of MA influence charge recombination, even though MA does not contribute to electron or hole wave functions. The findings rationalize the unusual temperature dependence of carrier lifetimes in halide perovskites and emphasize inorganic lattice deformation and MA rotation during polaron formation. By detecting nontrivial correlations within complex data and providing accurate quantitative measures, machine learning surpasses traditional analyses and suggests that perovskite performance can be controlled by chemical changes that alter perovskite geometric structure.

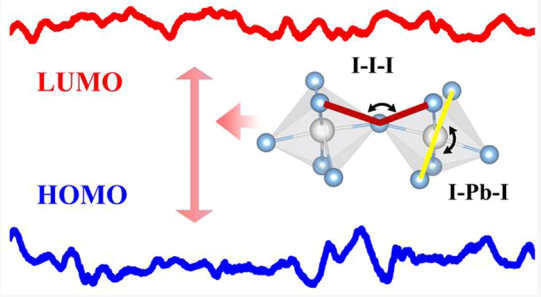

Hybrid organic−inorganic perovskite solar cells (PSCs) have attracted significant attention over the past decade because of their extraordinary properties, such as a high power conversion efficiency and the ease and low cost of production.[1−6] Halide perovskites are promising materials for next-generation photovoltaic devices due to long electron and hole lifetimes, large charge diffusion lengths, low defect densities, and high absorption coefficients.[6−8] Applications of perovskites extend beyond solar energy into light-emitting diodes.[9−14] The efficiency of PSCs has exceeded 23%.[1,15] Tremendous efforts continue to be dedicated to enhancing their efficiency, improving their stability, and reducing their environmental impact, by employing different synthesis methods,[16−18] adapting new device architectures,[19,20] and trying various stoichiometries.[10,21,22] Multiple experiments have been dedicated to understanding the unique combination of properties that make PSCs so efficient.[6,23−26] The unusual charge carrier dynamics and their response to nuclear motions are among the main factors determining the performance of PSCs. Multiple theoretical efforts have focused on elucidating the geometric and electronic structure of perovskites, focusing on different stoichiometries, dimensionalities (three-dimensional vs two-dimensional vs quantum dots), and defects (vacancies, interstitials, dopants, grain boundaries, and interfaces).[7,21,27−30] Theoretical studies of the quantum dynamics of coupled electronic and nuclear degrees of freedom are still rare, because they require advanced computational techniques.[31−34] Analysis and interpretation of simulation results constitute an additional challenge, in particular, due to the complex landscape of perovskite compositions, structures, and length and time scales involved.

Machine learning (ML) has emerged as a useful tool for analyzing both large and limited amounts of data available from either experiment or modeling, with applications in an extremely diverge range of fields, including high-energy physics, chemistry and materials science, social sciences, politics, etc.[35−38] Often, ML allows scientists to uncover trends and correlations that are hard to anticipate *a priori*. Quantum dynamics of charge carrier trapping and recombination in perovskites is an excellent candidate for ML analysis, because of the multitude of factors influencing carrier lifetimes, including the perovskite composition, thermodynamic phase, defects, geometric and electronic structure, temperature,

Received: April 27, 2020
Accepted: May 15, 2020
Published: May 15, 2020

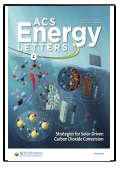

https://dx.doi.org/10.1021/acsenergylett.0c00899
ACS Energy Lett. 2020, 5, 1930−1938

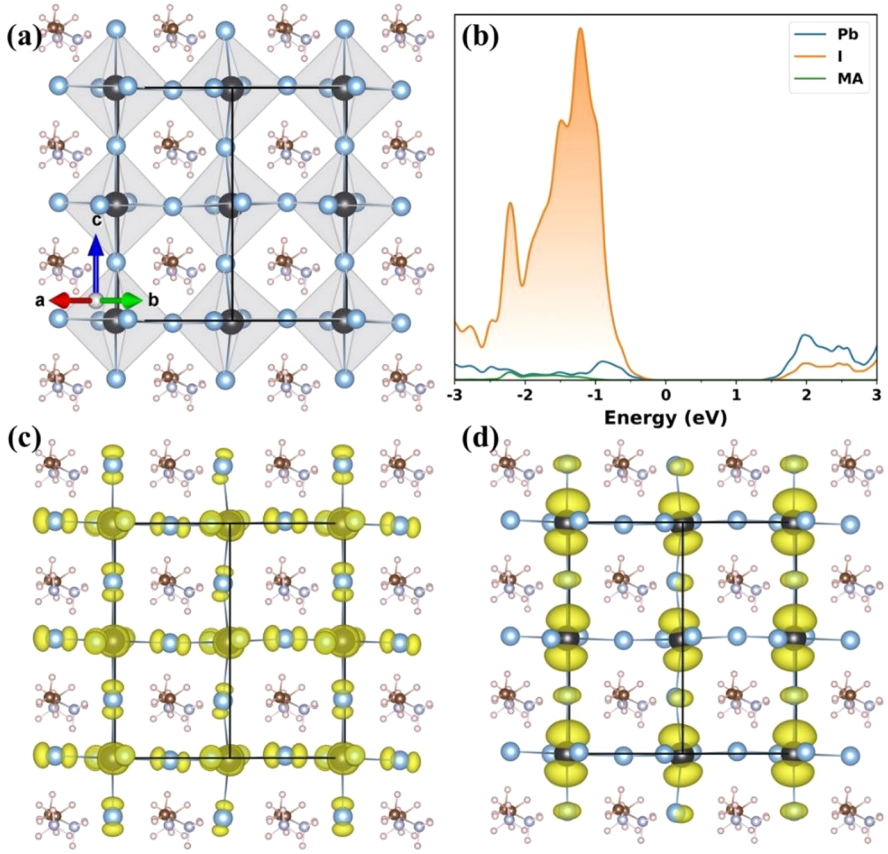

Figure 1. Geometric and electronic structure of $MAPbI_3$. (a) Tetragonal phase of $MAPbI_3$ (tetragonal primitive unit cell). (b) Projected density of states showing inorganic, Pb and I, and organic, CH_3NH_3 (MA), contributions. (c) HOMO and (d) LUMO charge densities, localized primarily on I and Pb, respectively.

atomic motions, electron−phonon coupling, quantum coherence, etc. Generally, ML techniques can be categorized into supervised and unsupervised learning.[38] Computational studies of nanoscale materials, and perovskites in particular, can benefit from both approaches. For example, supervised learning can be used to obtain efficient neural-network force fields trained to *ab initio* density functional theory (DFT),[39,40] while unsupervised learning can uncover complex reaction paths.[41] ML techniques help resolve the complex dependence problem and have attracted a great deal of attention from material scientists, because they provide analysis and modeling tools that outperform the traditional methods in terms of accuracy and efficiency.

Nonadiabatic molecular dynamics (MD) simulation combined with time-dependent DFT (TDDFT) has recently established itself as a tool of choice for modeling the complex highly non-equilibrium evolution of coupled electronic and nuclear degrees of freedom in molecular, nanoscale, and condensed matter systems.[32,33,42−45] Nonadiabatic MD treats all particles and interactions explicitly and at the atomistic level and avoids approximations used in phenomenological theories, such as harmonic phonons, weak system−bath interaction, few-level models, and adjustable parameters. By generating a time-domain description of excited state quantum dynamics, nonadiabatic MD combined with TDDFT mimics directly multiple time-resolved pump−probe spectroscopies while at the same time taking explicit account of the realistic aspects of material structure, including the chemical composition, defects, dopants, surfaces, interfaces, grain boundaries, etc.[46] The *ab initio* time-domain simulations can be easily transferred to new types of materials. Because such simulations produce large amounts of data, it is natural to consider ML as a data analysis tool.

In this Letter, we apply unsupervised ML to *ab initio* nonadiabatic MD and demonstrate that nonradiative charge carrier losses in $MAPbI_3$ are governed primarily by a material's structural properties rather than particular phonon motions. This fact is unexpected because the nonadiabatic electron−phonon coupling depends explicitly on nuclear velocity. Also unexpectedly, we find that MA motions have a strong influence on the nonradiative relaxation, even though MA does not contribute to the electron or hole wave functions. The main influence arises from the geometry of the inorganic Pb−I sublattice, with the I−I−I angle providing a stronger measure of electron−phonon coupling and the bandgap than the Pb−I−Pb tilt angle. These findings rationalize the unusual temperature dependence of charge carrier lifetimes in halide perovskites[47] and support the mechanism of polaron formation involving Pb−I lattice distortion and MA rotation. Our study highlights the ability of ML to uncover important correlations that are not anticipated *a priori* within complex data sets and shows that it can provide important quantitative measures with limited amounts of data. The reported findings suggest that the performance of PSCs can be improved by engineering of perovskite geometric structure using site substitution, doping, mixed stoichiometries, and related synthetic techniques.

We study pristine tetragonal $MAPbI_3$ represented by one 48-atom 1 × 1 × 1 supercell as shown in Figure 1a and a larger

https://dx.doi.org/10.1021/acsenergylett.0c00899
ACS Energy Lett. 2020, 5, 1930−1938

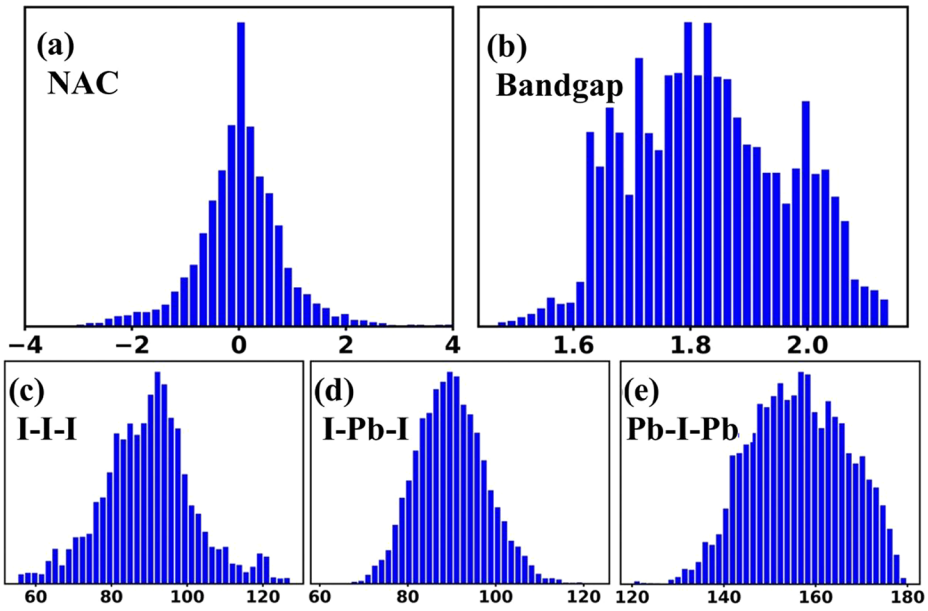

Figure 2. Probability distributions of (a) the NAC between HOMO and LUMO (millielectronvolts), (b) the bandgap (electronvolts), and (c) I−I−I, (d) I−Pb−I, and (e) Pb−I−Pb angles (degrees). These angles have the highest mutual information with the NAC and bandgap among all considered geometric features and atomic motions.

384-atom 2 × 2 × 2 supercell to check the convergence of the results. The 1 × 1 × 1 tetragonal phase is represented using a $\sqrt{2} \times \sqrt{2} \times 2$ unit cell of the cubic phase. DFT and ground state MD simulations are performed with the Vienna Ab initio Simulation Package (VASP),[48−51] employing the Perdew−Burke−Ernzerhof (PBE) exchange-correlation functional[52] and projector-augmented wave (PAW) method.[53] We use a 4 × 4 × 2 Monkhorst−Pack k-point mesh to sample the Brillouin zone for structure optimization, static calculation, and MD simulation. For the 2 × 2 × 2 supercell, we use only the Γ-point due to the computational cost. The optimized structure has a 1.63 eV bandgap and lattice constants a = 8.8 Å and c = 12.685 Å, in good agreement with the previous publications and experimental values.[54,55] Because $MAPbI_3$ has a direct bandgap at the Γ-point and we focus on the electron−hole recombination across the fundamental bandgap, only the wave function from the Γ-point is used to compute the nonadiabatic coupling (NAC) for the ML analysis. The crystal is first optimized and then thermalized at 300 K by velocity rescaling. Then, a 9 ps *ab initio* MD trajectory is generated with a 1 fs time step, and the NAC between HOMO and LUMO at the Γ-point is computed using the PYthon eXtension for Ab Initio Dynamics (PYXAID) code.[32,33] The PYXAID methodology has been used previously to model successfully excited dynamics in a broad range of materials.[42−44,56−66] The results of the quantum dynamics calculations performed with PYXAID on halide perovskites also show good agreement with the experimental data.[45−47,67−75] Generally, the time scales and mechanisms of charge carrier dynamics depend on the energy gap, NAC, and coherence time between pairs of states. The latter can be computed from autocorrelation of the energy gap.[76] Therefore, we focus on the gap and the NAC and apply ML to analyze how they depend on atomistic features and motions of $MAPbI_3$.

A total of 44 features are considered for both the 1 × 1 × 1 supercell and the 2 × 2 × 2 supercell, including 22 static and 22 dynamic features, as shown in Table SI and Figure S1. The dynamic features are time derivatives of the static features. The 22 static features, including bond lengths, bond angles, dihedral angles, relative orientations, and distances, are represented by 207 specific internal coordinates in the 48-atom system. For example, there are four C−N bonds from the four MA molecules representing the C−N bond distance feature. As a result, 414 static and dynamic variables are extracted from the MD trajectory. Correspondingly, the 384-atom systems contains 2720 internal coordinates representing static variables and the same amount of dynamic variables. The top 10 features are selected and discussed in detail. The ML analysis demonstrates that the importance of the structural and dynamic parameters drops rapidly within the set of 44 features, with the 10th most important feature already being 1.5−1.6 times less important than the top feature. Figure 2 shows distributions of the top three features (bond angles within the inorganic sublattice of $MAPbI_3$) and the target variables (NAC and bandgap). The 414 and 5440 variables and the target variables obtained from the MD trajectories for the 1 × 1 × 1 and 2 × 2 × 2 supercells are normalized individually to remove bias and artificial variance introduced by the choice of units. After that, the pairwise mutual information (MI)

$$I(X, Y) = \iint \mathrm{d}x\ \mathrm{d}y\ p(x, y) \log_2\left[\frac{p(x, y)}{p(x)p(y)}\right] \quad (1)$$

between each feature and each target variable is estimated using the K-nearest neighbor (KNN) algorithm.[77,78] In addition, the entropy is estimated as

$$H(X) = -\int \mathrm{d}x\ p(x) \log_2[p(x)] \quad (2)$$

and the MI is normalized by dividing by the entropy of the corresponding target variable. In eqs 1 and 2, $p(x, y)$ is the joint density distribution of continuous random variables X and Y and $p(x)$ and $p(y)$ are their densities. The results of the KNN algorithm calculations reported below use k = 3. We have tested different values of k and observed similar results. A

https://dx.doi.org/10.1021/acsenergylett.0c00899
ACS Energy Lett. 2020, 5, 1930−1938

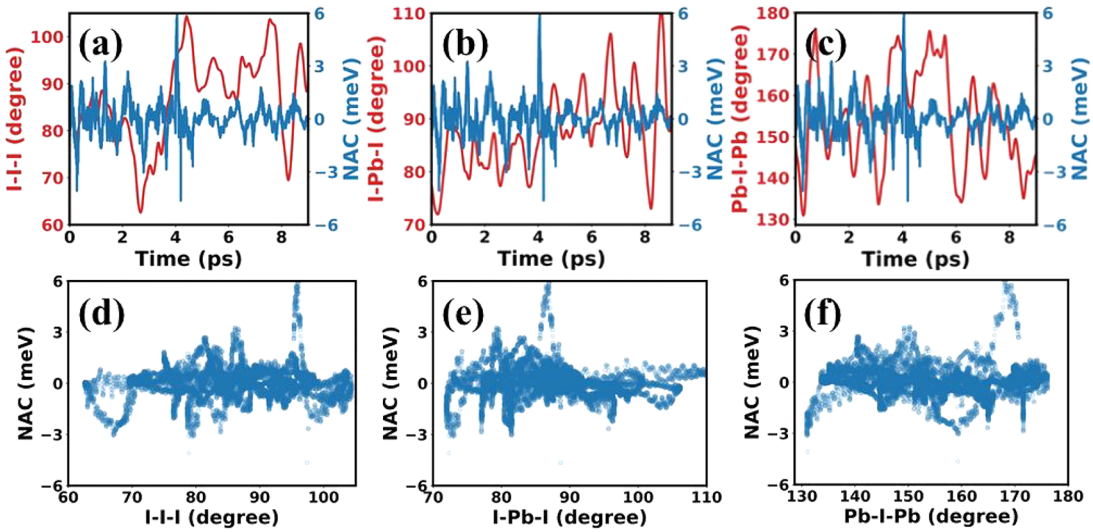

Figure 3. Evolution of (a) I−I−I, (b) I−Pb−I (90°), and (c) Pb−I−Pb angles superimposed with evolution of the NAC between HOMO and LUMO. (d−f) Joint distributions of these three angles with NAC.

Table 1. Mutual Information Values of Internal Coordinates and Motions with NAC

	I−I−I angle	I−Pb−I (90°) angle	Pb−I−Pb angle	I−Pb−I (180°) angle	Pb−I−Pb motion
rank	1	2	3	4	5
MI	0.87 ± 0.05	0.73 ± 0.06	0.71 ± 0.07	0.63 ± 0.04	0.62 ± 0.06
MI/H	0.48 ± 0.03	0.39 ± 0.04	0.39 ± 0.04	0.34 ± 0.03	0.34 ± 0.04
	MA−axis c angle	I−Pb−I (90°) motion	MA−MA angle	MA−MA distance	MA−a axis angle
rank	6	7	8	9	10
MI	0.61 ± 0.08	0.60 ± 0.05	0.60 ± 0.03	0.59 ± 0.02	0.59 ± 0.04
MI/H	0.33 ± 0.04	0.33 ± 0.03	0.33 ± 0.02	0.32 ± 0.01	0.32 ± 0.03

smaller k leads to a sharper fluctuant probability distribution but introduces noise/variance into the estimated MI. A larger k gives smoother densities; however, it is harder to differentiate contributions of different variables. The computed MI values for these 414 and 5440 individual variables are used to average across the variables for each feature type, to obtain the final MI values for each feature. The details of evaluating the MI are provided in the Supporting Information.

Figure 1 characterizes the geometric and electronic structure of $MAPbI_3$ in its optimized geometry. The $MAPbI_3$ bandgap falls within the solar spectrum, which is a necessary condition for solar energy applications. Spatial separation of electrons and holes is one of the reasons for the fantastic performance of PSC. The valence band edge arises mostly from atomic orbitals of iodine atoms, while the conduction band edge from lead atoms. The sparse structure of the inorganic Pb−I lattice, containing sufficiently large cavities to accommodate MA and similar molecules, ensures that the level of overlap of the atomic orbitals supporting electrons and holes is small, compared with those of the more conventional two-component semiconductors, such as TiO_2 and CdSe, and pure elements, such as Si. The small level of overlap ensures a small NAC and a short quantum coherence time, favoring long-lived charge carriers.[21,28,47]

Figure 2 presents canonical distributions of the NAC and the bandgap, as well as the three most important $MAPbI_3$ features that share the highest MI with the NAC and the bandgap. These distributions are broad and roughly Gaussian, implying that thermal fluctuations of the lattice have a strong impact on the electronic system, motivating us to search for correlations of lattice coordinates and motions with the electronic properties. Considering each panel in Figure 2, we note that the NAC is indeed very small, usually less than 2 meV. However, the NAC has fairly long tails that may have a significant influence on charge carrier recombination, because the recombination rate depends on NAC^2, for instance, according to Fermi's golden rule.[79] The bandgap fluctuates by ∼0.5 eV at 300 K. The fluctuation is large because the conduction and valence band edges originate from spatially separated and weakly interacting atomic orbitals (Figure 1). The large bandgap fluctuation gives rise to a short quantum coherence for electron−hole recombination.[76] A short coherence slows quantum dynamics and extends carrier lifetimes.[80] The I−I−I and I−Pb−I angles form Gaussian distributions around 90° (Figure 2c,d), with the former exhibiting a larger fluctuation. The Pb−I−Pb angle is notably <180°. This octahedral tilt angle plays an important role in polaron formation.[81,82]

One can attempt to establish a relationship of the NAC and the bandgap with geometric features and motions of $MAPbI_3$ using linear models. However, even though each individual feature has a trivial Gaussian-like distribution, their joint distributions are complicated, and there is no obvious linear dependence between them. Figure 3 presents the time evolution and joint distributions for the three coordinates with the NAC. The NAC fluctuates faster than the coordinates, which vary more slowly and smoothly. The largest absolute value of the correlation coefficient between the geometric features and the NAC is <0.32, with the majority of the correlation coefficients being around 0.1−0.2. The fairly

https://dx.doi.org/10.1021/acsenergylett.0c00899
ACS Energy Lett. 2020, 5, 1930−1938

Table 2. Mutual Information Values of Internal Coordinates with the Bandgap

	I−I−I angle	I−Pb−I (90°) angle	Pb−I−Pb angle	MA−*c* axis angle	I−Pb−I (180°) angle
rank	1	2	3	4	5
MI	2.31 ± 0.09	1.99 ± 0.11	1.96 ± 0.14	1.72 ± 0.16	1.69 ± 0.07
MI/*H*	1.17 ± 0.05	1.00 ± 0.06	0.99 ± 0.07	0.87 ± 0.08	0.85 ± 0.04
	MA−MA angle	MA−MA distance	MA−*a* axis angle	Pb−I distance	
rank	6	7	8	9	
MI	1.67 ± 0.13	1.62 ± 0.06	1.56 ± 0.12	1.47 ± 0.09	
MI/H	0.84 ± 0.07	0.82 ± 0.03	0.79 ± 0.06	0.74 ± 0.05	

computationally expensive 9 ps *ab initio* MD trajectory provides 9000 data points, which is sufficient to evaluate the probability distributions for individual properties (Figure 2) and to converge nonadiabatic MD calculations. However, the joint distributions are distorted (Figure 3d−f), making it harder to determine the contributions from the atomic features to the target variables.

Unsupervised learning techniques can extract hidden complex information from limited data, providing an important advantage over the traditional analyses. Tables 1 and 2 show the most important internal coordinates and motions that have the highest MI with the NAC and the bandgap, respectively. The entropies of the NAC and the bandgap are 1.84 ± 0.04 and 1.98 ± 0.04, respectively, which are close to the value of the standard normal distribution $\log_2(2\pi e)/2 = 2.05$. The MI is used to quantify the shared information between two random variables. The I−I−I angle shares the highest information with the NAC and the bandgap (MI = 0.87 ± 0.05 and 2.31 ± 0.09, respectively). The MI values are much larger than the MI of the bivariate normal distribution [$\mathrm{MI} = -\log_2(1 - \rho^2)/2 < 0.07$], calculated using the correlation coefficient $|\rho| < 0.32$ in our data set (Figure 3d). This result points to the complex and significant interdependence of these features and demonstrates the invalidity of the linear correlation.

The top 10 features exhibiting the highest MI with the NAC (Table 1) include, in decreasing importance, the following: I−I−I bond angle, I−Pb−I bond angle (∼90°), Pb−I−Pb bond angle, I−Pb−I bond angle (∼180°), angular velocity of the Pb−I−Pb bond angle, MA orientation relative to the lattice vector *c* (Figure 1), angular velocity of the I−Pb−I bond angle (∼90°), relative angle between two neighboring MA molecules, center-of-mass distance between two neighboring MA molecules, and orientation of MA relative to the lattice vector *a*. These 10 most important features are selected by the unsupervised learning from the set of 44 features, including internal coordinates and motions of bond lengths, bond angles, and dihedral angles in the inorganic Pb−I lattice and MA molecules, as well as the orientations of MA and distances between them. The bond angles within the inorganic lattice have the highest MI among all features. Note that while the Pb−I−Pb tilt angle, frequently used in perovskite structure analysis,[81,82] belongs to the top 10 features, the I−I−I angle provides a better measure of the impact of lattice distortion on charge carrier dynamics. The tilt and I−I−I angles together describe the relative orientation of the PbI_6 octahedra blocks, and the I−Pb−I angles (90° and 180°) describe the shape of the PbI_6 octahedra. This is consistent with the data depicted in Figure 1. The HOMO and LUMO of the system are localized on the inorganic lattice. Therefore, the NAC between these orbitals is mostly determined by the lattice angles. The results presented above suggest that modifying the structure of the PbI_6 octahedra block, for instance, by strain, temperature, chemical composition, or doping, should influence the carrier dynamics.

Perhaps most surprisingly, the ML analysis indicates that the $MAPbI_3$ lattice motions are much less important than the $MAPbI_3$ structure. Only two motions are present among the top 10 features in Table 1. This result is unexpected, because the NAC depends explicitly on nuclear velocity $\dot{\boldsymbol{R}}$:

$$\mathrm{NAC} = -i\hbar\left\langle \phi_i \middle| \frac{\mathrm{d}}{\mathrm{d}t} \middle| \phi_j \right\rangle = -i\hbar\left\langle \phi_i | \nabla_{\boldsymbol{R}} | \phi_j \right\rangle \cdot \dot{\boldsymbol{R}} \tag{3}$$

This expression separates the influence of the velocity and overlap contributions. The ML data demonstrate that the overlap-type matrix element $\langle \phi_i | \nabla_{\boldsymbol{R}} | \phi_j \rangle$ is more important for the charge carrier dynamics in $MAPbI_3$ than the nuclear velocity. This fact explains the unusual temperature dependence of the charge carrier lifetimes.[47,83] The velocity dependence of the NAC suggests that charge carrier lifetimes should decrease with an increase in temperature, because a higher temperature implies a higher kinetic energy and faster motions and a larger NAC, leading to faster charger carrier relaxation. Instead, the lifetime increases with temperature,[83] because thermal fluctuations induce lattice distortions and decrease $\langle \phi_i | \nabla_{\boldsymbol{R}} | \phi_j \rangle$.[47]

Also surprisingly, four of the top 10 features involve MA molecules (Table 1), even though they do not contribute to the valence or conduction band edges (Figure 1b). These molecules influence the charge carrier dynamics in two ways. Carrying a total positive charge and having a non-uniform charge distribution, they interact with electrons and holes electrostatically. Rotations of MA molecules contribute strongly to polaron formation,[81,82,84−86] screen electron−hole interactions,[87,88] and influence the ion diffusion that is responsible for the current−voltage hysteresis.[89] The screening facilitates electron−hole separation, reduces the extent of charge carrier recombination, and increases the carrier lifetime. In addition to the long-range electrostatic effects, MA molecules couple to the inorganic lattice by short-range repulsive steric interactions and affect electron−hole dynamics indirectly by distorting the inorganic lattice. The internal coordinates of the MA molecules contribute little to the carrier dynamics, and their MI with the NAC and the bandgap is small. Internal stretching and bending MA motions have little effect on electrostatic or steric interactions.

Table 2 presents the MI between the internal coordinates and the bandgap. The motions of the internal coordinates are not taken into consideration, because they do not affect the bandgap, in particular, because the DFT energy terms do not depend on nuclear velocities. Table 2 leads to conclusions similar to those reached on the basis of Table 1. The I−I−I angle shares the largest MI with the bandgap, just as with the NAC. The orientation and shape of the PbI_6 block, as well as

https://dx.doi.org/10.1021/acsenergylett.0c00899
ACS Energy Lett. 2020, 5, 1930−1938

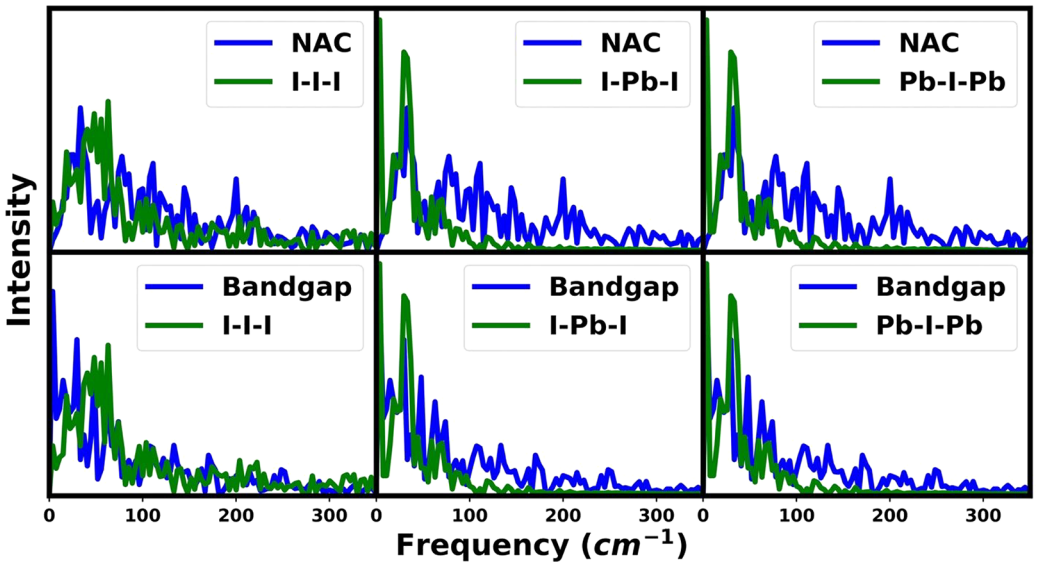

Figure 4. NAC and bandgap spectra compared with spectra of the key internal coordinates: I−I−I, I−Pb−I (90°), and Pb−I−Pb angles.

the orientation of MA molecules, are the most important factors affecting the electronic properties of the system. The last entry in Table 2 is the Pb−I bond length, which is not included in Table 1. The MI values drop significantly after these nine most important features, and we do not present them here.

The top 10 features obtained from the larger 384-atom 2 × 2 × 2 supercell and the smaller 48-atom 1 × 1 × 1 supercell are nearly identical, as shown in Tables SIII−SV. Most importantly, the first three features are the same for the two supercells and for the two target variables, the NAC and bandgap. The top seven of 10 features sorted on the basis of MI with NAC are all internal coordinates rather than motions. The results confirm that the I−I−I angle is the more important structural parameter governing the nonadiabatic charge recombination in $MAPbI_3$ and that structural deformation has a stronger influence on the charge recombination than particular atomic motions. A key difference between the results of the larger and smaller simulations is in the Pb−Pb distance, characterizing the relative distance between neighboring octahedra. The Pb−Pb distance is not in the top 10 list for the smaller system, but it takes the fourth place for the correlation with NAC and bandgap in the larger system, as shown in Tables SIII and SV. The difference arises due to the strong correlation between the nearby Pb atoms in the 1 × 1 × 1 system, which reduces the level of deformation of the octahedral blocks and does not represent properly fluctuations between the octahedra, as reflected in the Pb−Pb distance. This results in a reduced contribution of the Pb−Pb distance to the NAC and bandgap in the smaller system. Lahnsteiner et al. demonstrated[90] artificial correlations in small $MAPbI_3$ simulation cells affecting both Pb−Pb deformation and MA orientation. Proper treatment of correlations between MA dipoles may require very large simulation cells, because the dipoles may form ferroelectric domains. The results obtained with the 2 × 2 × 2 supercell demonstrate that deformations of octahedral blocks, as represented by the I−I−I, I−Pb−I, and Pb−I−Pb angles and the Pb−Pb distance, play a key role in the nonradiative carrier relaxation in $MAPbI_3$.

Another traditional empirical way to evaluate the influence of various coordinates and motions on the NAC and the bandgap is go to the frequency domain. Figure 4 shows Fourier transforms (FTs) of the phonon-induced fluctuations of the NAC and the bandgap along the *ab initio* MD trajectory, superimposed with the FTs of the three main angles. The spectra overlap significantly, indicating further that the bandgap and the NAC are correlated to these three features. In all cases, the strongest FT signals arise in the low-frequency region (<100 cm^{-1}). The FT of the I−I−I angle fluctuation matches best the higher-frequency part of the NAC and bandgap FTs, while the I−Pb−I and Pb−I−Pb angles provide a better match at the lower frequencies. The NAC exhibits stronger signals at the higher frequencies compared to the bandgap, because the NAC is a higher-order property than energy and is sensitive to a broader range of motions.

In conclusion, we have reported a ML analysis of the NAC and the energy gap that determine nonradiative charge carrier lifetimes in $MAPbI_3$. The study shows that $MAPbI_3$ structure, rather than its motions, governs most strongly the electron−phonon interactions that are responsible for charge carrier losses. This result is surprising, because the NAC depends explicitly on nuclear velocity, and therefore, faster and larger amplitude motions should enhance nonradiative relaxation. This result rationalizes, in particular, the unusual temperature dependence of charge carrier lifetimes in halide perovskites. The losses of charge are accelerated at higher temperatures in most materials; however, they are slowed in $MAPbI_3$ because of increased structural deformations. Only two motions are present among the top 10 $MAPbI_3$ features governing nonradiative charge recombination. The most important features stem from the inorganic Pb−I lattice as expected, because electrons and holes are localized primarily on Pb and I atoms. Unexpectedly, four of the 10 features involve rotations and displacements of MA species, which make no contribution to the conduction and valence band edges of $MAPbI_3$. This finding can be explained by direct long-range electrostatic interactions between charge carries and the MA cation and indirectly by short-range steric interactions between MA and the Pb−I lattice. Internal motions of MA have little influence on the charges.

ML provides a better tool than simple regression models for analyzing problems with complex dependencies. ML gives

https://dx.doi.org/10.1021/acsenergylett.0c00899
ACS Energy Lett. 2020, 5, 1930−1938

quantitative results that are hard to generate with traditional methods such comparing spectral densities. ML performs well with limited amounts of data, when spectral densities and correlations show significant noise. This is particularly valuable with costly *ab initio* time-domain simulations. The noise is partially eliminated during the calculation of MI by the summation or integration. The results of the unsupervised learning analysis with MI demonstrate the capability of extracting critical factors affecting carrier losses PSC. The fact that structural deformations of the inorganic lattice are the most important among all of the dynamic and static features in PSC suggests that the PSC performance can be engineered by doping or site substitutions affecting the structure. The ML analysis shows that the I−I−I angle provides a better measure than the Pb−I−Pb tilt angle when studying the effects from these modifications on charge carrier lifetimes.

■ ASSOCIATED CONTENT

Supporting Information

The Supporting Information is available free of charge at https://pubs.acs.org/doi/10.1021/acsenergylett.0c00899.

Description of the theoretical methodology, list of static and dynamic features used in the ML analysis, pictorial illustration of these features, details of the unsupervised ML calculations, and complete tables of mutual information of the bandgap and NAC with these features for the 1 × 1 × 1 and 2 × 2 × 2 simulation supercells (PDF)

■ AUTHOR INFORMATION

Corresponding Author

Oleg V. Prezhdo − *Department of Physics and Astronomy and Department of Chemistry, University of Southern California, Los Angeles, California 90089, United States;* orcid.org/0000-0002-5140-7500; Email: prezhdo@usc.edu

Authors

Guoqing Zhou − *Department of Physics and Astronomy, University of Southern California, Los Angeles, California 90089, United States;* orcid.org/0000-0002-4000-8467

Weibin Chu − *Department of Chemistry, University of Southern California, Los Angeles, California 90089, United States;* orcid.org/0000-0001-5951-0337

Complete contact information is available at: https://pubs.acs.org/10.1021/acsenergylett.0c00899

Notes

The authors declare no competing financial interest.

■ ACKNOWLEDGMENTS

The work was supported by U.S. National Science Foundation Grant CHE-1900510.

■ REFERENCES

(1) Rong, Y. G.; Hu, Y.; Mei, A. Y.; Tan, H. R.; Saidaminov, M. I.; Seok, S. I.; McGehee, M. D.; Sargent, E. H.; Han, H. W. Challenges for Commercializing Perovskite Solar Cells. *Science* **2018**, *361*, eaat8235.

(2) Xing, G.; Mathews, N.; Sun, S.; Lim, S. S.; Lam, Y. M.; Grätzel, M.; Mhaisalkar, S.; Sum, T. C. Long-Range Balanced Electron-and Hole-Transport Lengths in Organic-Inorganic $CH_3NH_3PbI_3$. *Science* **2013**, *342*, 344−347.

(3) Green, M. A.; Ho-Baillie, A. Perovskite Solar Cells: The Birth of a New Era in Photovoltaics. *ACS Energy Lett.* **2017**, *2*, 822−830.

(4) Manser, J. S.; Christians, J. A.; Kamat, P. V. Intriguing Optoelectronic Properties of Metal Halide Perovskites. *Chem. Rev.* **2016**, *116*, 12956−13008.

(5) Brenner, T. M.; Egger, D. A.; Kronik, L.; Hodes, G.; Cahen, D. Hybrid Organic—Inorganic Perovskites: Low-Cost Semiconductors with Intriguing Charge-Transport Properties. *Nat. Rev. Mater.* **2016**, *1*, 15007.

(6) Herz, L. M. Charge-Carrier Mobilities in Metal Halide Perovskites: Fundamental Mechanisms and Limits. *Acs Energy Lett.* **2017**, *2*, 1539−1548.

(7) Yin, W. J.; Yang, J. H.; Kang, J.; Yan, Y. F.; Wei, S. H. Halide Perovskite Materials for Solar Cells: A Theoretical Review. *J. Mater. Chem. A* **2015**, *3*, 8926−8942.

(8) Liang, P. W.; Liao, C. Y.; Chueh, C. C.; Zuo, F.; Williams, S. T.; Xin, X. K.; Lin, J. J.; Jen, A. K. Y. Additive Enhanced Crystallization of Solution-Processed Perovskite for Highly Efficient Planar-Heterojunction Solar Cells. *Adv. Mater.* **2014**, *26*, 3748−3754.

(9) Wu, Y.; Li, X.; Zeng, H. Highly Luminescent and Stable Halide Perovskite Nanocrystals. *ACS Energy Lett.* **2019**, *4*, 673−681.

(10) Yang, W. S.; Park, B.-W.; Jung, E. H.; Jeon, N. J.; Kim, Y. C.; Lee, D. U.; Shin, S. S.; Seo, J.; Kim, E. K.; Noh, J. H.; Seok, S. I. Iodide Management in Formamidinium-Lead-Halide−Based Perovskite Layers for Efficient Solar Cells. *Science* **2017**, *356*, 1376−1379.

(11) Tan, Z. K.; Moghaddam, R. S.; Lai, M. L.; Docampo, P.; Higler, R.; Deschler, F.; Price, M.; Sadhanala, A.; Pazos, L. M.; Credgington, D.; et al. Bright Light-Emitting Diodes Based on Organometal Halide Perovskite. *Nat. Nanotechnol.* **2014**, *9*, 687−692.

(12) Li, G. R.; Tan, Z. K.; Di, D. W.; Lai, M. L.; Jiang, L.; Lim, J. H. W.; Friend, R. H.; Greenham, N. C. Efficient Light-Emitting Diodes Based on Nanocrystalline Perovskite in a Dielectric Polymer Matrix. *Nano Lett.* **2015**, *15*, 2640−2644.

(13) Yantara, N.; Bhaumik, S.; Yan, F.; Sabba, D.; Dewi, H. A.; Mathews, N.; Boix, P. P.; Demir, H. V.; Mhaisalkar, S. Inorganic Halide Perovskites for Efficient Light-Emitting Diodes. *J. Phys. Chem. Lett.* **2015**, *6*, 4360−4364.

(14) Miyano, K.; Tripathi, N.; Yanagida, M.; Shirai, Y. Lead Halide Perovskite Photovoltaic as a Model P-I-N Diode. *Acc. Chem. Res.* **2016**, *49*, 303−310.

(15) Huang, J.; Yuan, Y.; Shao, Y.; Yan, Y. Understanding the Physical Properties of Hybrid Perovskites for Photovoltaic Applications. *Nat. Rev. Mater.* **2017**, *2*, 17042.

(16) Luo, D. Y.; Yang, W. Q.; Wang, Z. P.; Sadhanala, A.; Hu, Q.; Su, R.; Shivanna, R.; Trindade, G. F.; Watts, J. F.; Xu, Z. J.; et al. Enhanced Photovoltage for Inverted Planar Heterojunction Perovskite Solar Cells. *Science* **2018**, *360*, 1442−1446.

(17) Parvazian, E.; Abdollah-Zadeh, A.; Akbari, H. R.; Taghavinia, N. Fabrication of Perovskite Solar Cells Based on Vacuum-Assisted Linear Meniscus Printing of $MAPbI_3$. *Sol. Energy Mater. Sol. Cells* **2019**, *191*, 148−156.

(18) Correa-Baena, J.-P.; Saliba, M.; Buonassisi, T.; Grätzel, M.; Abate, A.; Tress, W.; Hagfeldt, A. Promises and Challenges of Perovskite Solar Cells. *Science* **2017**, *358*, 739−744.

(19) Kwon, H. C.; Yang, W.; Lee, D.; Ahn, J.; Lee, E.; Ma, S.; Kim, K.; Yun, S. C.; Moon, J. Investigating Recombination and Charge Carrier Dynamics in a One-Dimensional Nanopillared Perovskite Absorber. *ACS Nano* **2018**, *12*, 4233−4245.

(20) Fang, Y.; Bi, C.; Wang, D.; Huang, J. The Functions of Fullerenes in Hybrid Perovskite Solar Cells. *ACS Energy Lett.* **2017**, *2*, 782−794.

(21) Li, Z.; Kolodziej, C.; McCleese, C.; Wang, L.; Kovalsky, A.; Samia, A. C.; Zhao, Y.; Burda, C. Effect of Chloride Substitution on Interfacial Charge Transfer Processes in $MAPbI_3$ Perovskite Thin Film Solar Cells: Planar Versus Mesoporous. *Nanoscale Adv.* **2019**, *1*, 827−833.

(22) Aranda, C.; Guerrero, A.; Bisquert, J. Ionic Effect Enhances Light Emission and Photovoltage of Methylammonium Lead Bromide

Perovskite Solar Cell by Reduced Surface Recombination. *ACS Energy Lett.* **2019**, *4*, 741−746.
(23) Liu, M. Z.; Johnston, M. B.; Snaith, H. J. Efficient Planar Heterojunction Perovskite Solar Cells by Vapour Deposition. *Nature* **2013**, *501*, 395−398.
(24) Zhou, H. P.; Chen, Q.; Li, G.; Luo, S.; Song, T. B.; Duan, H. S.; Hong, Z. R.; You, J. B.; Liu, Y. S.; Yang, Y. Interface Engineering of Highly Efficient Perovskite Solar Cells. *Science* **2014**, *345*, 542−546.
(25) Yang, W. S.; Noh, J. H.; Jeon, N. J.; Kim, Y. C.; Ryu, S.; Seo, J.; Seok, S. I. High-Performance Photovoltaic Perovskite Layers Fabricated through Intramolecular Exchange. *Science* **2015**, *348*, 1234−1237.
(26) Burschka, J.; Pellet, N.; Moon, S. J.; Humphry-Baker, R.; Gao, P.; Nazeeruddin, M. K.; Gratzel, M. Sequential Deposition as a Route to High-Performance Perovskite-Sensitized Solar Cells. *Nature* **2013**, *499*, 316−319.
(27) Du, M. H. Efficient Carrier Transport in Halide Perovskites: Theoretical Perspectives. *J. Mater. Chem. A* **2014**, *2*, 9091−9098.
(28) Wang, Y. T.; Fang, W. H.; Long, R.; Prezhdo, O. V. Symmetry Breaking at $MAPbI_3$ Perovskite Grain Boundaries Suppresses Charge Recombination: Time-Domain Ab Initio Analysis. *J. Phys. Chem. Lett.* **2019**, *10*, 1617−1623.
(29) He, J. L.; Vasenko, A. S.; Long, R.; Prezhdo, O. V. Halide Composition Controls Electron-Hole Recombination in Cesium-Lead Halide Perovskite Quantum Dots: A Time Domain Ab Lnitio Study. *J. Phys. Chem. Lett.* **2018**, *9*, 1872−1879.
(30) Chakraborty, S.; Xie, W.; Mathews, N.; Sherburne, M.; Ahuja, R.; Asta, M.; Mhaisalkar, S. G. Rational Design: A High-Throughput Computational Screening and Experimental Validation Methodology for Lead-Free and Emergent Hybrid Perovskites. *ACS Energy Lett.* **2017**, *2*, 837−845.
(31) Craig, C. F.; Duncan, W. R.; Prezhdo, O. V. Trajectory Surface Hopping in the Time-Dependent Kohn-Sham Approach for Electron-Nuclear Dynamics. *Phys. Rev. Lett.* **2005**, *95*, 163001.
(32) Akimov, A. V.; Prezhdo, O. V. The Pyxaid Program for Non-Adiabatic Molecular Dynamics in Condensed Matter Systems. *J. Chem. Theory Comput.* **2013**, *9*, 4959−4972.
(33) Akimov, A. V.; Prezhdo, O. V. Advanced Capabilities of the Pyxaid Program: Integration Schemes, Decoherenc:E Effects, Multi-excitonic States, and Field-Matter Interaction. *J. Chem. Theory Comput.* **2014**, *10*, 789−804.
(34) Wang, L. J.; Akimov, A.; Prezhdo, O. V. Recent Progress in Surface Hopping: 2011−2015. *J. Phys. Chem. Lett.* **2016**, *7*, 2100−2112.
(35) Lo, Y. C.; Rensi, S. E.; Torng, W.; Altman, R. B. Machine Learning in Chemoinformatics and Drug Discovery. *Drug Discovery Today* **2018**, *23*, 1538−1546.
(36) Bertone, G.; Deisenroth, M. P.; Kim, J. S.; Liem, S.; de Austri, R. R.; Welling, M. Accelerating the BSM Interpretation of LHC Data with Machine Learning. *Phys. Dark Universe* **2019**, *24*, 100293.
(37) Yu, Y. Z.; Tan, X. H.; Ning, S. G.; Wu, Y. Y. Machine Learning for Understanding Compatibility of Organic-Inorganic Hybrid Perovskites with Post-Treatment Amines. *ACS Energy Lett.* **2019**, *4*, 397−404.
(38) Butler, K. T.; Davies, D. W.; Cartwright, H.; Isayev, O.; Walsh, A. Machine Learning for Molecular and Materials Science. *Nature* **2018**, *559*, 547−555.
(39) Smith, J. S.; Isayev, O.; Roitberg, A. E. Ani-1: An Extensible Neural Network Potential with DFT Accuracy at Force Field Computational Cost. *Chem. Sci.* **2017**, *8*, 3192−3203.
(40) Ghasemi, S. A.; Hofstetter, A.; Saha, S.; Goedecker, S. Interatomic Potentials for Ionic Systems with Density Functional Accuracy Based on Charge Densities Obtained by a Neural Network. *Phys. Rev. B: Condens. Matter Mater. Phys.* **2015**, *92*, 045131.
(41) Tavadze, P.; Avendaño Franco, G.; Ren, P.; Wen, X.; Li, Y.; Lewis, J. P. A Machine-Driven Hunt for Global Reaction Coordinates of Azobenzene Photoisomerization. *J. Am. Chem. Soc.* **2018**, *140*, 285−290.
(42) Prezhdo, O. V. Multiple Excitons and the Electron-Phonon Bottleneck in Semiconductor Quantum Dots: An Ab Initio Perspective. *Chem. Phys. Lett.* **2008**, *460*, 1−9.
(43) Wang, L. J.; Long, R.; Prezhdo, O. V. Time-Domain Ab Initio Modeling of Photoinduced Dynamics at Nanoscale Interfaces. *Annu. Rev. Phys. Chem.* **2015**, *66*, 549−579.
(44) Long, R.; Prezhdo, O. V.; Fang, W. H. Nonadiabatic Charge Dynamics in Novel Solar Cell Materials. *Wiley Interdiscip. Rev.: Comput. Mol. Sci.* **2017**, *7*, e1305.
(45) Zhou, X.; Jankowska, J.; Dong, H.; Prezhdo, O. V. Recent Theoretical Progress in the Development of Perovskite Photovoltaic Materials. *J. Energy Chem.* **2018**, *27*, 637−649.
(46) Li, W.; Long, R.; Tang, J. F.; Prezhdo, O. V. Influence of Defects on Excited-State Dynamics in Lead Halide Perovskites: Time-Domain Ab Initio Studies. *J. Phys. Chem. Lett.* **2019**, *10*, 3788−3804.
(47) Li, W.; Tang, J. F.; Casanova, D.; Prezhdo, O. V. Time-Domain Ab Lnitio Analysis Rationalizes the Unusual Temperature Dependence of Charge Carrier Relaxation in Lead Halide Perovskite. *ACS Energy Lett.* **2018**, *3*, 2713−2720.
(48) Kresse, G. Ab-Initio Molecular-Dynamics for Liquid-Metals. *J. Non-Cryst. Solids* **1995**, *193*, 222−229.
(49) Kresse, G.; Hafner, J. Ab-Initio Molecular-Dynamics Simulation of the Liquid-Metal Amorphous-Semiconductor Transition in Germanium. *Phys. Rev. B: Condens. Matter Mater. Phys.* **1994**, *49*, 14251−14269.
(50) Kresse, G.; Furthmuller, J. Efficiency of Ab-Initio Total Energy Calculations for Metals and Semiconductors Using a Plane-Wave Basis Set. *Comput. Mater. Sci.* **1996**, *6*, 15−50.
(51) Kresse, G.; Furthmuller, J. Efficient Iterative Schemes for Ab Initio Total-Energy Calculations Using a Plane-Wave Basis Set. *Phys. Rev. B: Condens. Matter Mater. Phys.* **1996**, *54*, 11169−11186.
(52) Perdew, J. P.; Burke, K.; Ernzerhof, M. Generalized Gradient Approximation Made Simple. *Phys. Rev. Lett.* **1996**, *77*, 3865−3868.
(53) Blochl, P. E. Projector Augmented-Wave Method. *Phys. Rev. B: Condens. Matter Mater. Phys.* **1994**, *50*, 17953−17979.
(54) Leguy, A. M.; Azarhoosh, P.; Alonso, M. I.; Campoy-Quiles, M.; Weber, O. J.; Yao, J.; Bryant, D.; Weller, M. T.; Nelson, J.; Walsh, A.; van Schilfgaarde, M.; Barnes, P. R. F. Experimental and Theoretical Optical Properties of Methylammonium Lead Halide Perovskites. *Nanoscale* **2016**, *8*, 6317−6327.
(55) Baikie, T.; Fang, Y.; Kadro, J. M.; Schreyer, M.; Wei, F.; Mhaisalkar, S. G.; Graetzel, M.; White, T. J. Synthesis and Crystal Chemistry of the Hybrid Perovskite $(CH_3NH_3)PbI_3$ for Solid-State Sensitised Solar Cell Applications. *J. Mater. Chem. A* **2013**, *1*, 5628−5641.
(56) Zhang, L. L.; Vasenko, A. S.; Zhao, J.; Prezhdo, O. V. Mono-Elemental Properties of 2D Black Phosphorus Ensure Extended Charge Carrier Lifetimes under Oxidation: Time-Domain Ab Initio Analysis. *J. Phys. Chem. Lett.* **2019**, *10*, 1083−1091.
(57) Li, L. Q.; Long, R.; Prezhdo, O. V. Why Chemical Vapor Deposition Grown MoS_2 Samples Outperform Physical Vapor Deposition Samples: Time-Domain Ab Initio Analysis. *Nano Lett.* **2018**, *18*, 4008−4014.
(58) Zhang, Z. S.; Liu, L. H.; Fang, W. H.; Long, R.; Tokina, M. V.; Prezhdo, O. V. Plasmon-Mediated Electron Injection from Au Nanorods into MoS_2: Traditional Versus Photoexcitation Mechanism. *Chem.* **2018**, *4*, 1112−1127.
(59) Pal, S.; Casanova, D.; Prezhdo, O. V. Effect of Aspect Ratio on Multiparticle Auger Recombination in Single-Walled Carbon Nanotubes: Time Domain Atomistic Simulation. *Nano Lett.* **2018**, *18*, 58−63.
(60) Zhou, X.; Jankowska, J.; Li, L. Q.; Giri, A.; Hopkins, P. E.; Prezhdo, O. V. Strong Influence of Ti Adhesion Layer on Electron-Phonon Relaxation in Thin Gold Films: Ab Initio Nonadiabatic Molecular Dynamics. *ACS Appl. Mater. Interfaces* **2017**, *9*, 43343−43351.
(61) Long, R.; Casanova, D.; Fang, W. H.; Prezhdo, O. V. Donor−Acceptor Interaction Determines the Mechanism of Photo-induced Electron Injection from Graphene Quantum Dots into TiO_2:

https://dx.doi.org/10.1021/acsenergylett.0c00899
ACS Energy Lett. 2020, 5, 1930−1938

π-Stacking Supersedes Covalent Bonding. *J. Am. Chem. Soc.* **2017**, *139*, 2619−2629.
(62) Akimov, A. V.; Muckerman, J. T.; Prezhdo, O. V. Nonadiabatic Dynamics of Positive Charge During Photocatalytic Water Splitting on GaN(10−10) Surface: Charge Localization Governs Splitting Efficiency. *J. Am. Chem. Soc.* **2013**, *135*, 8682−8691.
(63) Chaban, V. V.; Prezhdo, V. V.; Prezhdo, O. V. Covalent Linking Greatly Enhances Photoinduced Electron Transfer in Fullerene-Quantum Dot Nanocomposites: Time-Domain Ab Initio Study. *J. Phys. Chem. Lett.* **2013**, *4*, 1−6.
(64) Fischer, S. A.; Duncan, W. R.; Prezhdo, O. V. Ab Initio Nonadiabatic Molecular Dynamics of Wet-Electrons on the TiO_2 Surface. *J. Am. Chem. Soc.* **2009**, *131*, 15483−15491.
(65) Lu, T. F.; Wang, Y. S.; Tomko, J. A.; Hopkins, P. E.; Zhang, H. X.; Prezhdo, O. V. Control of Charge Carrier Dynamics in Plasmonic Au Films by Tiox Substrate Stoichiometry. *J. Phys. Chem. Lett.* **2020**, *11*, 1419−1427.
(66) Yang, Y. T.; Fang, W. H.; Benderskii, A.; Long, R.; Prezhdo, O. V. Strain Controls Charge Carrier Lifetimes in Monolayer WSe_2: Ab Initio Time Domain Analysis. *J. Phys. Chem. Lett.* **2019**, *10*, 7732−7739.
(67) He, J.; Fang, W.-H.; Long, R.; Prezhdo, O. V. Increased Lattice Stiffness Suppresses Nonradiative Charge Recombination in $MAPbI_3$ Doped with Larger Cations: Time-Domain Ab Initio Analysis. *ACS Energy Lett.* **2018**, *3*, 2070−2076.
(68) Li, W.; Liu, J.; Bai, F.-Q.; Zhang, H.-X.; Prezhdo, O. V. Hole Trapping by Iodine Interstitial Defects Decreases Free Carrier Losses in Perovskite Solar Cells: A Time-Domain Ab Initio Study. *ACS Energy Lett.* **2017**, *2*, 1270−1278.
(69) Li, W.; Vasenko, A. S.; Tang, J. F.; Prezhdo, O. V. Anharmonicity Extends Carrier Lifetimes in Lead Halide Perovskites at Elevated Temperatures. *J. Phys. Chem. Lett.* **2019**, *10*, 6219−6226.
(70) Tong, C. J.; Li, L. Q.; Liu, L. M.; Prezhdo, O. V. Synergy between Ion Migration and Charge Carrier Recombination in Metal-Halide Perovskites. *J. Am. Chem. Soc.* **2020**, *142*, 3060−3068.
(71) He, J. L.; Fang, W. H.; Long, R.; Prezhdo, O. V. Superoxide/Peroxide Chemistry Extends Charge Carriers' Lifetime but Undermines Chemical Stability of $CH_3NH_3PbI_3$ Exposed to Oxygen: Time-Domain Ab Initio Analysis. *J. Am. Chem. Soc.* **2019**, *141*, 5798−5807.
(72) Zhang, Z. S.; Fang, W. H.; Long, R.; Prezhdo, O. V. Exciton Dissociation and Suppressed Charge Recombination at 2D Perovskite Edges: Key Roles of Unsaturated Halide Bonds and Thermal Disorder. *J. Am. Chem. Soc.* **2019**, *141*, 15557−15566.
(73) Long, R.; Prezhdo, O. V. Dopants Control Electron-Hole Recombination at Perovskite-TiO_2 Interfaces: Ab Initio Time-Domain Study. *ACS Nano* **2015**, *9*, 11143−11155.
(74) Li, W.; Liu, J.; Bai, F. Q.; Zhang, H. X.; Prezhdo, O. V. Hole Trapping by Iodine Interstitial Defects Decreases Free Carrier Losses in Perovskite Solar Cells: A Time-Domain Ab Initio Study. *ACS Energy Lett.* **2017**, *2*, 1270−1278.
(75) Liu, J.; Prezhdo, O. V. Chlorine Doping Reduces Electron-Hole Recombination in Lead Iodide Perovskites: Time-Domain Ab Initio Analysis. *J. Phys. Chem. Lett.* **2015**, *6*, 4463−4469.
(76) Akimov, A. V.; Prezhdo, O. V. Persistent Electronic Coherence Despite Rapid Loss of Electron-Nuclear Correlation. *J. Phys. Chem. Lett.* **2013**, *4*, 3857−3864.
(77) Kraskov, A.; Stogbauer, H.; Grassberger, P. Estimating Mutual Information. *Phys. Rev. E* **2004**, *69*, No. 066138.
(78) Khan, S.; Bandyopadhyay, S.; Ganguly, A. R.; Saigal, S.; Erickson, D. J.; Protopopescu, V.; Ostrouchov, G. Relative Performance of Mutual Information Estimation Methods for Quantifying the Dependence among Short and Noisy Data. *Phys. Rev. E* **2007**, *76*, No. 026209.
(79) Hyeon-Deuk, K.; Madrid, A. B.; Prezhdo, O. V. Symmetric Band Structures and Asymmetric Ultrafast Electron and Hole Relaxations in Silicon and Germanium Quantum Dots: Time-Domain Ab Initio Simulation. *Dalton Trans.* **2009**, 10069−10077.
(80) Kilina, S. V.; Neukirch, A. J.; Habenicht, B. F.; Kilin, D. S.; Prezhdo, O. V. Quantum Zeno Effect Rationalizes the Phonon Bottleneck in Semiconductor Quantum Dots. *Phys. Rev. Lett.* **2013**, *110*, 180404.
(81) Mahata, A.; Meggiolaro, D.; De Angelis, F. From Large to Small Polarons in Lead, Tin, and Mixed Lead-Tin Halide Perovskites. *J. Phys. Chem. Lett.* **2019**, *10*, 1790−1798.
(82) Miyata, K.; Meggiolaro, D.; Trinh, M. T.; Joshi, P. P.; Mosconi, E.; Jones, S. C.; De Angelis, F.; Zhu, X. Y. Large Polarons in Lead Halide Perovskites. *Science Advances* **2017**, *3*, No. e1701217.
(83) Milot, R. L.; Eperon, G. E.; Snaith, H. J.; Johnston, M. B.; Herz, L. M. Temperature-Dependent Charge-Carrier Dynamics in $CH_3NH_3PbI_3$ Perovskite Thin Films. *Adv. Funct. Mater.* **2015**, *25*, 6218−6227.
(84) Ambrosio, F.; Wiktor, J.; De Angelis, F.; Pasquarello, A. Origin of Low Electron-Hole Recombination Rate in Metal Halide Perovskites. *Energy Environ. Sci.* **2018**, *11*, 101−105.
(85) Neukirch, A. J.; Nie, W. Y.; Blancon, J. C.; Appavoo, K.; Tsai, H.; Sfeir, M. Y.; Katan, C.; Pedesseau, L.; Even, J.; Crochet, J. J.; et al. Polaron Stabilization by Cooperative Lattice Distortion and Cation Rotations in Hybrid Perovskite Materials. *Nano Lett.* **2016**, *16*, 3809−3816.
(86) Park, M.; Neukirch, A. J.; Reyes-Lillo, S. E.; Lai, M. L.; Ellis, S. R.; Dietze, D.; Neaton, J. B.; Yang, P. D.; Tretiak, S.; Mathies, R. A. Excited-State Vibrational Dynamics toward the Polaron in Methylammonium Lead Iodide Perovskite. *Nat. Commun.* **2018**, *9*, 2525.
(87) Even, J.; Pedesseau, L.; Katan, C. Analysis of Multivalley and Multibandgap Absorption and Enhancement of Free Carriers Related to Exciton Screening in Hybrid Perovskites. *J. Phys. Chem. C* **2014**, *118*, 11566−11572.
(88) Zhu, H. M.; Miyata, K.; Fu, Y. P.; Wang, J.; Joshi, P. P.; Niesner, D.; Williams, K. W.; Jin, S.; Zhu, X. Y. Screening in Crystalline Liquids Protects Energetic Carriers in Hybrid Perovskites. *Science* **2016**, *353*, 1409−1413.
(89) Tong, C. J.; Geng, W.; Prezhdo, O. V.; Liu, L. M. Role of Methylammonium Orientation in Ion Diffusion and Current Voltage Hysteresis in the $CH_3NH_3PbI_3$ Perovskite. *ACS Energy Lett.* **2017**, *2*, 1997−2004.
(90) Lahnsteiner, J.; Kresse, G.; Kumar, A.; Sarma, D.; Franchini, C.; Bokdam, M. Room-Temperature Dynamic Correlation between Methylammonium Molecules in Lead-Iodine Based Perovskites: An Ab Initio Molecular Dynamics Perspective. *Phys. Rev. B: Condens. Matter Mater. Phys.* **2016**, *94*, 214114.

https://dx.doi.org/10.1021/acsenergylett.0c00899
ACS Energy Lett. 2020, 5, 1930−1938